# Facile preparation of $CuBi_2O_4/TiO_2$ hetero-systems employed for simulated solar-light selective oxidation of 4-methoxybenzyl alcohol model compound

Ahmed Malek Djaballah[a], Marianna Bellardita*[,b], Leonardo Palmisano[b], Vittorio Loddo[b], Claudio Maria Pecoraro[b], Radia Bagtache[a], Mohamed Trari[c]

[a] Laboratory of Electrochemistry-Corrosion, Metallurgy and Inorganic Chemistry, Faculty of Chemistry, (USTHB), BP 32, 16111, Algiers, Algeria

[b] Engineering Department, University of Palermo, Viale delle Scienze Ed. 6, 90128, Palermo, Italy

[c] Laboratory of Storage and Valorisation of Renewable Energies, Faculty of Chemistry, (USTHB), BP 32, 16111, Algiers, Algeria

## Abstract

Photocatalytic selective oxidation of organics is today considered as one of the green techniques for the synthesis of important starting materials for different technological applications. This work reports an efficient, simple, and cheap strategy for the synthesis of a new $CuBi_2O_4$-$TiO_2$ (CBO/$TiO_2$) photocatalytic hetero-system at room temperature. The prepared powders were characterized by X-ray diffraction (XRD), UV-Vis diffuse reflectance spectra (DRS), field-emission scanning electron microscopy (FE-SEM), X-ray photoelectron spectroscopy (XPS), and electrochemical measurements. The photocatalytic activity was evaluated by performing a probe reaction, i.e., the partial oxidation of 4-methoxybenzyl alcohol (4-MBA) to 4-methoxybenzaldehyde (4-MBAld) in water solution under simulated solar light irradiation. The photoactivity of the CBO/$TiO_2$ coupled systems was higher than that of the single photocatalysts reaching a selectivity towards 4-methoxy-benzaldehyde of 45% with an alcohol conversion of 77% after 4h of irradiation. Moreover, although high conversion of the alcohol was achieved, the selectivity towards 4-MBAld was significant, differently from what described in literature where it has been reported for many heterogeneous photocatalytic reactions that selectivity generally decreases significantly with increasing conversion of the starting molecule. The improved photocatalytic activity could be attributed to the partial coverage of the $TiO_2$ surface by CBO that reduces the successive oxidation of the formed aldehyde.

**Keywords**:

Heterogeneous photocatalysis, $CuBi_2O_4/TiO_2$ ($CBO/TiO_2$) hetero-system, Selective alcohol oxidation, Simulated solar light.

## 1- Introduction

The green energy industries are growing rapidly with the global energy crisis and can be considered as alternatives to the traditional processes to contribute to global energy supply and environmental protection. Consequently, the green partial oxidation of alcohols is a beneficial process from both an industrial and research point of view [1–3]. Traditionally, the synthesis of aldehydes is based on oxidizing alcohols in halogenated solvents [4], or using strong oxidants such as hypochlorite, Cr(IV), chlorine, and peracids which are harmful chemical agents [5,6]. In recent years, photo-induced oxidation has attracted much attention owing to the environmentally friendly processes under mild experimental conditions [7,8]. With appropriate design of efficient photocatalysts, the substrates oxidation could be performed by photo-generated charges [9]. The photo-generated electrons and holes in the presence of molecular oxygen ($O_2$) produce reactive species e.g., superoxide anion radicals ($^{\bullet}O^{2-}$) and hydroxyl radicals ($^{\bullet}OH$) which can induce several redox reactions such as the oxidation of alcohols [10]. Recently, several attempts have been devoted to developing transition metal oxide catalysts e.g., $WO_3$ [11], $TiO_2$ [12–15], structured spinel as $CuBi_2O_4$ and perovskite as $BaTiO_3$, not only for pollutant degradation but also for the partial oxidation of alcohols due to their low cost, reproducibility, stability, and good photocatalytic activity [10,16,17]. In particular, great research effort has been devoted to the use of spinel $CuBi_2O_4$ in electrochemical [18,19] and chemical [20,21] processes. It has been shown that in both processes the efficiency of $CuBi_2O_4$ is related with the existence of $Cu^{2+}$ species and oxygen vacancies on its surface. However, the application of $TiO_2$-based photocatalysts is hampered due to the ineffective use of solar energy and the short lifetime of the photogenerated electron-hole pairs [22]. The coupling of different semiconductors represents one of the most useful ways to overcome the above limitations for practical applications of the photocatalytic method [23,24]. Very few studies have analysed the photoactivity of transition metal spinels combined with $TiO_2$ [20,25–29]. The purpose of this research is to demonstrate the outstanding effect of the coexistence of $CuBi_2O_4$ and $TiO_2$ particles in the field of organic synthesis. In particular, the selective photocatalytic oxidation of 4-methoxybenzyl alcohol, as model compound, by using CBO/$TiO_2$ hetero-system in the presence of $O_2$ under both UV-light and simulated solar light irradiation has been investigated. We focused on the synthesis and the photocatalytic performance of CBO/$TiO_2$ hetero-systems with different mass ratios through an inexpensive, easy and reproducible ball milling method.

## 2-Experimental

### *2.1. Materials*

Copper(II) nitrate trihydrate $Cu(NO_3)_2 \cdot 3H_2O$ (Merck > 98 %), bismuth(III) nitrate pentahydrate $Bi(NO_3)_3 \cdot 5H_2O$ (Merck > 98%), titanium tetrachloride (Fluka 98%), 4-methoxybenzyl alcohol (Fluka 98%), 4-methoxybenzaldehyde (98% Sigma-Aldrich), 4-methoxybenzoic acid (98% Sigma-Aldrich), potassium hydroxide (Fluka 65%), trifluoroacetic acid (Merck > 98 %), acetonitrile (ACN, UV HPLC grade Sigma-Aldrich > 99.9 %), acetic acid (≥ 99%), absolute ethanol (EtOH, 99.7%), sodium sulfate ($Na_2SO_4$) and hydrochloric acid (HCl, 37%) were purchased from Scharlab. All chemicals were used as received without further purification along with ultrapure deionized water during this study.

### *2.2. Catalysts*

#### *2.2.1. Synthesis of $CuBi_2O_4$*

$CuBi_2O_4$ (CBO) was synthesized by a very facile co-precipitation method following the nitrate route. Cu $(NO_3)_2 \cdot 3H_2O$ (Merck > 98 %), and $Bi(NO_3)_3 \cdot 5H_2O$ (Merck > 98%) were mixed in stoichiometric proportions and dissolved in 50 ml distilled water. The mixture, after adjusting the pH at 12.20 with KOH, was heated in air at 140 °C for 48 hours. The solid was recovered by filtration, washed with water, and dried at 60 °C.

#### *2.2.2. Synthesis of $TiO_2$*

The precursor was titanium tetrachloride (Fluka 98%), which was not further purified. It was slowly added to distilled water at room temperature (molar ratio Ti/$H_2O$ 1:60; volume ratio 1:10). After 12 hours of continuous stirring at room temperature a clear solution was obtained and it was boiled under stirring for 0.5 h. This treatment yielded a milky white $TiO_2$ dispersion, which was dried under vacuum at 323 K. The code of this sample is HP-$TiO_2$.

#### *2.2.3. Synthesis of $CuBi_2O_4$/$TiO_2$ hetero-system*

The two powders of $CuBi_2O_4$ and $TiO_2$ were mixed in different weight ratios, such as 2, 3, 4 and 5% and named X%$CuBi_2O_4$/HP-$TiO_2$ (X% indicates the $CuBi_2O_4$ weight percentage). The powders were kept inside a chrome steel jar coated with zirconium oxide and filled with 6 zirconium oxide balls, and ground in the open air at room temperature for 2 h using a planetary ball mill (PM 100, Retsch-Allee 1-5, 42781 Haan, Germany) **(Fig. 1)** at a rotation speed of 150 rpm; only the sample containing 3% of $CuBi_2O_4$ was also prepared at 300 rpm. After the treatment the mixtures were hand ground. In the following the value of the rotation speed of the ball milling treatment will be reported in the code of the sample only for the sample prepared at 300 rpm.

For the sake of comparison, a composite sample was prepared by mixing at 150 rpm CBO with the commercial $TiO_2$ sample Aeroxide P25. 3%CBO/P25 was the code identifying it.

### *2.3. Catalysts characterization*

To check the phase purity of semiconductors, X-ray diffraction was performed using an XRD, Philips X'Pert Pro diffractometer apparatus equipped with Cu-Kα filtered with nickel (λ= 1.54059), and generator settings (45 kV, 40 mA) at a scan rate of 2° $min^{-1}$. The band gap (Eg) values were calculated from the UV-vis DRS spectra by the Kubelka-Munk and Tauc Plot method [30], by considering the photocatalysts as indirect semiconductors. The reflectance spectra have been recorded from 190 to 800 nm by means of a Jasco 650 spectrophotometer equipped with an integrating sphere, and $BaSO_4$ was used as standard. The specific surface areas (SSA) of the powders was calculated by a Flow Sorb 2300 apparatus (Micromeritics) by using the single-point BET method. The samples were degassed for 30 min at 523 K before the measurement. The ATR-FTIR spectrum was plotted between 400 and 4000 $cm^{-1}$ thanks to a Perkin Elmer FTIR spectrophotometer with a band width of 2 $cm^{-1}$. Scanning electron microscope (SEM) with a Schottky field emission was employed to examine the powder's morphology (JEOL JSM 7600F FESEM). X-ray photoelectron spectra (XPS) were acquired by an X-ray photoelectron spectrometer system (250Xi/ESCALAB, Thermo Fisher Scientific, United States) by using Al Kα radiation.

### *2.4. Photoelectrochemical measurement*

Photoelectrochemical measurements were carried out in 0.1 M ammonium pentaborate (ABE) aqueous solution (pH ≈ 9) in a three-electrode configuration cell. HP-$TiO_2$, CBO, and 3%CBO/HP-$TiO_2$ photocatalysts were drop casted on carbon paper support (Toray 40% wet

Proofed-E-Tek) and immersed in the ABE solution. A Pt wire was used as the counter electrode, and a silver/silver chloride (Ag/AgCl/sat. KCl) as the reference electrode (0 V vs Ag/AgCl = 0.197 V vs SHE). The photocurrent spectra were acquired by irradiating the samples through the quartz window of the cell using a 450 W UV-VIS Xenon lamp and a monochromator by varying the wavelength at fixed potential. A potentiostat was used to control the electrode potential, and the signal related to the measured current was sent to a two-phase lock-in amplifier to isolate the photocurrent from the overall current circulating in the cell. A mechanical chopper was used to stop the irradiation at a known frequency (namely 13 Hz). Flat bland potential was determined by plotting photocurrent versus applied potential at fixed wavelength (330 nm).

### *2.5. Photoreactivity experiments and adsorption measures*

The photocatalytic experiments were carried out in an annular Pyrex reactor, containing 500 mL of aqueous solution of 4-MBA, chosen as a model compound which is representative of aromatic alcohols. The initial concentration of 4-MBA was 0.5 mM, and the photocatalyst amount 1.5 g/L. A 50 W halogen lamp, placed in correspondence of the internal symmetry axis of the reactor, was used as the irradiation source. The lamp was switched on 30 min after the photocatalyst addition to the 4-MBA solution to ensure the achievement of the adsorption–desorption equilibrium of the substrate on the catalyst surface. During the photoreactivity tests, 3 ml of the reaction mixture were withdrawn at fixed times and immediately filtered through 0.2 µm membranes (HA, Millipore) to separate the photocatalyst particles before the HPLC analyses. The quantitative determination and identification of the starting molecule and its oxidation products were carried out using a Beckman Coulter HPLC (System Gold 126 Solvent Module and 168 Diode Array Detector), equipped with a Phenomenex Kinetex 5µ C18 (150mm × 4.6mm) column. The eluent consisted of a mixture of acetonitrile and 2 mM trifluoroacetic acid aqueous solution (20:80 volumetric ratio) and the flow rate was 0.8 mL $min^{-1}$. Retention times and UV spectra of the compounds were compared with those of standards. Adsorption measures of both alcohol and aldehyde were done to evaluate the interaction of the substrates with the catalyst. 0.15 g of CBO, HP-$TiO_2$ or 4% CBO/HP-$TiO_2$ 150 Rpm were added to 100 mL of a 0.5 mM aqueous solution of alcohol or aldehyde, and the dispersions were left in the dark under stirring for 2 hours to allow the adsorption of the substrates onto the catalyst surface. The conversion of alcohol, yield and selectivity towards aldehyde, during the photocatalytic runs were calculated with the following equations:

$$\text{Conversion \%} = [(C_0-C_1)/C_0] \cdot 100 \quad (1)$$

$$\text{Yield \%} = (C_2/C_0) \cdot 100 \quad (2)$$

$$\text{Selectivity \%} = [C_2/(C_0-C_1)] \cdot 100 \quad (3)$$

Where $C_0$, $C_1$ and $C_2$ represent the initial concentration of alcohol, the concentration of the alcohol and that of the aldehyde during the photocatalytic reaction, respectively,

## *3. Results and discussion*

### *3.1. XRD analysis*

The crystalline structure of all of the photocatalysts was determined through X-ray diffraction (XRD) recorded for 10 s at each 0.02° step over the 2θ interval 10–90°. The diffractograms of the home prepared HP-$TiO_2$, $CuBi_2O_4$ and $CuBi_2O_4$/HP-$TiO_2$ powders are displayed in **Fig. 2**. **Fig. 2a** shows that $TiO_2$ crystalline phase is prevalently anatase in a tetragonal crystal structure exposing the planes (101), (004), (200) (211), (204), (220) and (303) at 2θ values of 25.35°, 37.84°, 48.14°, 55.18°, 62.81°, 70.45° and 82.35° respectively, according to the JCPDS card No 89-4921. Rutile (plane (110) at 2θ=27.5°) is present as a minor component. XRD pattern reported in **Fig. 2b** shows that $CuBi_2O_4$ is present in a single-phase showing the characteristic main planes (with the maximum peaks intensity) (200), (211), (202), (400), (330), (312), (332) and (413) at 2θ values of 20.88°, 28.01°, 37.44°, 46.72°, 52.97°, 55.66°, 66.10°, and 78.27°

(JCPDS card No 42-0334), respectively. The structures of $TiO_2$ (HP) and the spinel $CuBi_2O_4$ (CBO) illustrated by the Vista software are reported in the inset of **Fig. 2a and 2b.**

The XRD pattern of 4%CBO/$TiO_2$ prepared at 150 Rpm was very similar to that of bare $TiO_2$ **(Fig. 2c)** indicating that the structure of this latter was not modified during the formation of the hetero-system with the $CuBi_2O_4$ spinel by ball milling treatment at 150 Rpm. Moreover, no CBO characteristic peaks were identified, due to the low CBO loading in the coupled system and the mild preparation conditions [31,32]. On the contrary, small differences with respect to bare $TiO_2$ can be noticed in the diffractogram of the 4%CBO/$TiO_2$ sample prepared at 300 Rpm, probably for the increase in temperature that occurs at the higher rotation speed during ball milling. In this case some weak peaks related to CBO are noticeable. All peaks are indexed in a tetragonal crystal structure with parameters lattices: a=8.499(6) Å and c=5.817(2) Å [10], confirming the formation of the spinel structure.

The size of nano crystallites (D = 2.54 nm) was evaluated from the Williamson Hall-plot **(Fig. 3)** from the full width at half maxima (β) of the strongest $TiO_2$ peak:

$$\beta cos\theta = (k\lambda/D) + 4\varepsilon\, sin\theta \quad (4)$$

### 3.2 Fourier Transform Infrared Spectroscopy (FTIR)

FTIR analysis is an effective method to analyse the composition and the surface characteristics of different materials. **Fig. 4** displays the FTIR spectra of the two bare and 4%$CuBi_2O_4$/HP-$TiO_2$ samples.

Bare $TiO_2$ displays two characteristic peaks. The first one at 1623.5 $cm^{-1}$ has been attributed to the Ti-O bending mode and to the water adsorbed on the surface of $TiO_2$ [33], the other at 3404 $cm^{-1}$ is related to the surface hydroxyl group (-OH) and can exhibit both symmetrical and asymmetrical stretching vibrations. In line with earlier reports, $CuBi_2O_4$ presents two strong peaks at 1386 and 554 $cm^{-1}$ that are caused by the stretching vibration of the Bi-O and Cu-O bonds, respectively. In the coupled 4%$CuBi_2O_4$/HP-$TiO_2$ the features of the two components are distinguishable with a slight shift of the band at 3404 $cm^{-1}$ attributable to the interaction between the two oxides.

### *3.3. UV–visible spectra analysis*

**Fig. 5a** exhibits the UV–VIS diffuse reflectance spectra of $CuBi_2O_4$, $TiO_2$ and CBO/HP-$TiO_2$ hetero-systems. $CuBi_2O_4$ shows an absorption edge in the visible range between 620 and 800 nm, due to its narrow bandgap and brown colour. Bare $TiO_2$ and all hetero-systems show a clear absorption edge at ca. 385 nm attributed to the band-to-band transition of $TiO_2$ [34–36]. The addition of CBO to $TiO_2$ enhances the light absorption in the visible region causing a reflectance decrease between 400 and 800 nm.

For an indirect-gap semiconductor, it is well known that the optical bandgap value is estimated with the help of the Kubelka-Munk method combined with the Tauc relation [31].

$$F(R_\infty) = a_\lambda = \frac{(1-R_\infty)^2}{2R_\infty} = \frac{\alpha}{S} \tag{5}$$

This method is based on the absorption coefficient ($\alpha_\lambda$, $cm^{-1}$) which is $\lambda$-dependent, $R_\infty$ is deduced from the diffuse reflectance data (R%). The Eg value is deduced from the extrapolation of the line with the hν-axis, expressed by the relation:

$$(\alpha h\nu)^{1/n} = K \times (h\nu - E_g) \tag{6}$$

Where $\alpha$ is the coefficient of absorption, hν the energy of photon, and $E_g$ the band gap. K is a proportionality constant, while the exponent n indicates the type of transition, equal to 2 and 0.5 for indirect and direct transition, respectively [37].

**In Fig. 5b** are plotted the values of $(\alpha h\nu)^{1/2}$ versus the incident photon energy (hν) by considering the hetero-structures as indirect semiconductors like the bare HP-$TiO_2$. The band gap values of the used photocatalysts, calculated from this plot, are reported in Table 1. Bare

HP-$TiO_2$ has a band gap of 3.20 eV typical of $TiO_2$ anatase, the majority phase, whilst CBO reveals a high absorption of visible light and displays a band gap of 1.88 eV. The coupled samples show almost the same band bap values of bare $TiO_2$ indicating that the interaction with the spinel does not modify the electronic structure of the oxide. Bare CBO displays a very low specific surface area value whilst bare $TiO_2$ has an area of ca. 76 $m^2$ $g^{-1}$. The coupled samples have generally a greater value than the corresponding bare support, and a reduction was noticed for the samples prepared a 300 rpm. The high rotation rate caused the formation of a more compact structure accordingly to SEM images (see further on).

**Table 1.** Some features of the used photocatalysts.

| Sample | Band-gap (eV) | S.S.A. ($m^2$ $g^{-1}$) |
|---|---|---|
| CBO | 1.88 | 2.1 |
| HP-$TiO_2$ | 3.20 | 105.5 |
| 2%CBO- HP-$TiO_2$ | 3.02 | 101.8 |
| 3%CBO- HP-$TiO_2$ | 2.98 | 104.5 |
| 4%CBO- HP-$TiO_2$ | 3.20 | 108.7 |
| 5%CBO- HP-$TiO_2$ | 3.20 | 104.9 |
| 4%CBO- HP-$TiO_2$ 300 rpm | 3.08 | 74.51 |
| 3%CBO-P25 | 3.16 | 63.2 |

***3.4. XPS analysis***

X-ray photoelectron spectroscopy was used to study the surface chemical composition and electronic core levels of the coupled samples to understand the valence status. In particular, in **Fig. 6** are reported the spectra of the 4%CBO/HP-$TiO_2$ sample as representative of the prepared mixtures. As it can be seen from the XPS survey spectrum in **Fig. 6a**, the composite clearly contains the Cu, Bi, Ti, O, elements in agreement with the EDX results. The electronic core levels of Cu 2p, Bi 4f, O 1s, and Ti 2p in CBO/HP-$TiO_2$ hetero-system were further studied by the high resolution XPS spectra.

The C signal observed at 284.6 eV comes from the amorphous carbon applied to calibrate the scale of binding energy in **Fig. 6**a [38]. The highly resolved spectrum of Ti 2p **(Fig. 6b)** presents two peaks centered at 459.3 eV and 465.0 eV, which could be attributed to Ti 2p3/2 and Ti 2p1/2 states [39]. These spin-orbit splitting states represents Ti-O bonding ($Ti^{+4}$) and are typical for $TiO_2$ [40]. Image in **Fig. 6c** displays the XPS spectrum of Bi 4f core level. The peaks at 159.7 and 164.1 eV are ascribed to Bi 4f7/2 and Bi 4f5/2, respectively. This result indicates that the bismuth species exists in the form of Bi-O bonding with trivalent oxidation state in the hetero-system [41].

In **Fig. 6d** is reported the spectrum of Cu 2p core level. The peaks at 933.8 is ascribed to the binding energies of $Cu^{2+}$ 2p, and the peaks at 941.8 and 928.4 eV are the satellite peaks of $Cu^{2+}$ [41,42]. Only one peak can be observed owing to the low content of Cu in $CuBi_2O_4/TiO_2$.

Moreover, the O 1s spectrum is reported in **Fig. 6e**, in which the peak at 525.9 eV (O1) can be assigned to lattice oxygen [43]. At the same time, the deconvoluted peak at 529.3 eV (O2) can be assigned to the surface hydroxyl groups (-OH), and the peak at the high binding energy of 532.7 eV (O3) to the adsorbed water. XPS analysis further confirms the co-existence of CBO and $TiO_2$ in the heterojunction.

### *3.5. SEM analysis*

The morphology of HP-$TiO_2$ and 4%CBO/HP-$TiO_2$ hetero-systems prepared at 150 and 300 rpm were explored by SEM analysis (**Fig. 7**). Bare $TiO_2$ (**Fig. 7a**) and bare CBO (**Fig. 7b)** consist of particles of different shape and morphology whose dimensions are in the range 10-500 nm. After the ball milling treatment **(Fig. 7c, d),** a decrease of the $TiO_2$ particles size can be noticed and the effect is more evident for the highest rotation speed. The distribution of the particles is uniform indicating a good mixing of the two components and the morphology is similar to that of the bare $TiO_2$. The energy dispersion spectrum (EDS) of 4%CBO/HP-$TiO_2$ 150 rpm confirms the presence of O, Ti, Cu and Bi **(Fig. 7e)**, with Cu and Bi present in small amounts in the coupled system. Furthermore, the EDS elemental mapping images **(Fig. 7f)** reveal the homogeneous distribution of the different elements supporting the successful formation of a mixed CBO and $TiO_2$ system.

### *3.6. Electrochemical properties*

Electrochemical characterizations were also assessed to study the electronic properties of the used photocatalysts to investigate the role of CBO in the hetero-structures. In **Fig. 8a and d** are reported the photocurrent spectra of the bare and 4%CBO/HP-$TiO_2$, recorded in 0.1 M ABE at the open circuit potential of 0.12 V vs and 0.22 V vs Ag/AgCl, for HP-$TiO_2$ and 4%CBO/ HP-$TiO_2$, respectively. For both the samples a maximum of photocurrent at 330 nm was recorded, this can be attributed to the low amount of CBO in the composite with respect to $TiO_2$. Negligible photocurrent values were recorded for pure CBO highlighting a poor mobility of charge carriers and/or the high recombination rate of the photogenerated charges. This finding can explain the practically inactivity of this samples (see photocatalytic results).

By considering a non-direct optical transition (n = 0.5), the optical band gap ($E_g$) values of the phocatalysts can be calculated by using the following Equation (11) [44]:

$$(Q_{ph} \cdot h\nu)^n \propto h\nu - E_g \tag{11}$$

where $h\nu$ is the photon energy and $Q_{ph}$ is the photocurrent yield. The latter is the measured photocurrent corrected for the efficiency of the lamp and it is proportional to the light absorption coefficient at $h\nu$ energy values near the band gap.

As shown in **Fig. 8b and e,** the optical band gaps are estimated by extrapolating to zero the $(Q_{ph}\ h\nu)^{0.5}$ vs $h\nu$ plots. The values are very similar for the two samples (that is 3.1eV for $TiO_2$

and 3.14 eV for 4%CBO/$TiO_2$), and in agreement with the experimental findings obtained by DRS. The presence of CBO does not modify the band gap of $TiO_2$.

The flat band potential ($E_{fb}$) is essential for predicting the $e^-$ and $h^+$ potentials and therefore the possible occurrence of determining redox reactions. $E_{fb}$ values, determined considering the potential value when the photocurrent vanishes (Fig. c and f), resulted similar for the two samples being -0.08 V for $TiO_2$ and -0.1 V for 4%CBO/$TiO_2$. The chrono-amperometry recorded by manually stopping the samples irradiation light (**inset Fig. 8**) is characteristic of *n*-type semiconductors.

### *3.7. Evaluation of photocatalytic performance: photocatalytic partial oxidation of 4-methoxybenzyl alcohol (4-MBA) under simulated solar light irradiation*

In order to investigate the effect of ball milling rotation rate, the photocatalytic performance of the samples 4% CBO/HP-$TiO_2$ 150 rpm and 4% CBO/HP-$TiO_2$ 300 rpm is compared in **Fig. 9**. At higher rpm a decrease of both conversion (46%), selectivity (33%) and yield (15%) were obtained, attributable to the more drastic synthesis conditions that induces modifications in the catalyst structure, as observed in the XRD pattern. For this reason, the samples containing different percentages of CBO were prepared at 150 rpm.

In **Fig. 10** the photocatalytic activity of the different samples towards the partial oxidation of 4-MBA is compared in term of alcohol conversion **(Fig. 10a)** and aldehyde selectivity **(Fig. 10b)** and yield **(Fig. 10c)** under simulated solar light irradiation. The alcohol conversion by using pristine CBO is very low whilst reaches values higher than 70% with the bare HP-$TiO_2$ and the different CBO/HP-$TiO_2$ composites. Interestingly, the coupling of CBO with HP-$TiO_2$ does not influence the oxidant power of the last, whilst higher selectivity and yield values were obtained. The best results were reached with the 4%CBO/HP-$TiO_2$ hetero-system with 77% of conversion, 45% selectivity and 35% yield. The presence of CBO changes the surface properties of $TiO_2$ favouring the aldehyde formation probably working similarly to $WO_3$ when coupled with $TiO_2$ [45]. In this case, the electronic features of CBO have a minor/negligible effect on the photocatalytic activity with respect to the surface ones since the partial coverage of the $TiO_2$ surface by the inactive CBO reduces the successive oxidation of the formed aldehyde.

Notably, the coupled samples revealed good performance even under simulated sunlight irradiation, paving the way for their large-scale use under direct solar irradiation [46]. It should also be noted that good selectivity was obtained despite the high alcohol conversion as generally high selectivity value are obtained at low conversion degree [47]. A continuous reactor could be used under direct solar irradiation in the presence of a selective membrane to separate the formed aldehyde, thus preventing its further oxidation.

These results confirm that the $CuBi_2O_4$/HP-$TiO_2$ coupled samples can be easily prepared by ball milling and used as promising photocatalysts for the selective oxidation of 4-MBA alcohol to the corresponding aldehyde.

Under simulated solar light irradiation both $TiO_2$ and CBO are excited by considering the conduction and band edges potential of the two oxides and the formation of a heterojunction cannot be ruled out, although the characterizations made did not allow us to definitively establish the presence of a heterojunction. We are more inclined to think, however, that the increase in selectivity in coupled samples is simply due to the fact that once the oxidation product, the aldehyde, is formed, the latter is released into the solution and its further oxidation on active sites of $TiO_2$ is reduced as the CBO on the surface limits it. The increased aldehyde production, in other words, can be attributed to the presence of the practically inactive CBO on the $TiO_2$ surface.

The dark adsorption measurements revealed similar percentages for 4-MBA on the three catalysts, whereas the aldehyde adsorption showed to be one order of magnitude lower on the composite sample (Table 3). This result strongly supports the higher selectivity obtained with coupled samples compared to bare $TiO_2$.

**Table 3.** Dark adsorption of 4-methoxybenzyl alcohol and 4-methoxybenzaldehyde on HP-$TiO_2$, CBO and 4% CBO/HP-$TiO_2$.

| **Catalysts** | **4-MBA Ads (%)** | **4-MBald Ads (%)** |
|---|---|---|
| HP-$TiO_2$ | 13 | 13 |
| CBO | 11 | 18 |
| 4% CBO/HP-$TiO_2$ | 7 | 0.9 |

## 4. Conclusions

In conclusion, CBO/HP-$TiO_2$ hetero-systems were successfully prepared using a simple and inexpensive mechanical ball milling method by mixing CBO with HP-$TiO_2$ powders for 2 h, in different weight ratios. The photoactivity of the composites was evaluated under simulated solar light irradiation by following the selective oxidation of 4-MBA towards 4-MBAld as a probe reaction. The method allowed to have a good interface contact and strong interaction between the two oxides, thus promoting absorption of visible light and enhancing separation and migration of photogenerated electron-hole pairs. The sample 4%CBO/HP-$TiO_2$ 150 rpm displayed the highest photoactivity with a conversion of 77%, a selectivity of 45% and a yield is 35% after 4 h under solar light irradiation by using water as the solvent. $^{\cdot}O_2^-$ and $h^+$ are the important oxidizing agents in the reaction system and CBO is essential to increase the selectivity without diminution in the conversion. A lower aldehyde adsorption on the composite samples was noticed with respect to the bare $TiO_2$, and this finding can justify the higher selectivity in the presence of the hetero-structured samples. The method used for obtaining them allowed large quantities of catalyst to be prepared in an economic, simple and rapid manner in view of a large-scale application using sunlight as an irradiation source.

## Acknowledgements

This contribution is dedicated to Prof. Rosario Pietropaolo, a visionary of science, master of ethics and dedication and inspiration for many of us.

## References

[1] L. Palmisano, V. Augugliaro, M. Bellardita, A. di Paola, E. García López, V. Loddo, G. Marcì, G. Palmisano, S. Yurdakal, Titania photocatalysts for selective oxidations in water, ChemSusChem. 4 (2011) 1431–1438. https://doi.org/10.1002/cssc.201100196.

[2] O. Tomita, T. Otsubo, M. Higashi, B. Ohtani, R. Abe, Partial Oxidation of Alcohols on Visible-Light-Responsive WO3 Photocatalysts Loaded with Palladium Oxide Cocatalyst, ACS Catal. 6 (2016) 1134–1144. https://doi.org/10.1021/acscatal.5b01850.

[3] S. Schünemann, M. van Gastel, H. Tüysüz, A cspbbr3/tio2 composite for visible-light-driven photocatalytic benzyl alcohol oxidation, ChemSusChem. 11 (2018) 2057–2061. https://doi.org/10.1002/cssc.201800679.

[4] T. Suzuki, Organic synthesis involving iridium-catalyzed oxidation, Chem Rev. 111 (2011) 1825–1845. https://doi.org/10.1021/cr100378r.

[5] A. Tetrahedron Lett, Readily Accessible 12-I-51 Oxidant for the Conversion of Primary and Secondary Alcohols to, Wiley, 1983. https://pubs.acs.org/sharingguidelines.

[6] A. Maleki, R. Rahimi, S. Maleki, Efficient oxidation and epoxidation using a chromium(VI)-based magnetic nanocomposite, Environ Chem Lett. 14 (2016) 195–199. https://doi.org/10.1007/s10311-016-0558-2.

[7] M. Bellardita, S. Yurdakal, B.S. Tek, C. Degirmenci, G. Palmisano, V. Loddo, L. Palmisano, J. Soria, J. Sanz, V. Augugliaro, Tuning the selectivity to aldehyde via pH regulation in the photocatalytic oxidation of 4-methoxybenzyl alcohol and vanillyl alcohol by TiO2catalysts, J Environ Chem Eng. 9 (2021). https://doi.org/10.1016/j.jece.2021.105308.

[8] T.P. Yoon, M.A. Ischay, J. Du, Visible light photocatalysis as a greener approach to photochemical synthesis, Nat Chem. 2 (2010) 527–532. https://doi.org/10.1038/nchem.687.

[9] M. Bellardita, M. Feilizadeh, R. Fiorenza, S. Scirè, L. Palmisano, V. Loddo, Selective aqueous oxidation of aromatic alcohols under solar light in the presence of TiO2

modified with different metal species, Photochemical and Photobiological Sciences. (2022). https://doi.org/10.1007/s43630-022-00284-2.

[10] A.M. Djaballah, R. Bagtache, S. Tartaya, M. Trari, Photoelectrochemical characterization of the hetero-junction Ag/CuBi2O4 application under visible light irradiation, Journal of Materials Science: Materials in Electronics. 33 (2022) 1555–1566. https://doi.org/10.1007/s10854-021-07673-w.

[11] O. Samuel, M.H.D. Othman, R. Kamaludin, O. Sinsamphanh, H. Abdullah, M.H. Puteh, T.A. Kurniawan, WO3–based photocatalysts: A review on synthesis, performance enhancement and photocatalytic memory for environmental applications, Ceram Int. 48 (2022) 5845–5875. https://doi.org/10.1016/j.ceramint.2021.11.158.

[12] Q. Guo, C. Zhou, Z. Ma, X. Yang, Fundamentals of TiO2 Photocatalysis: Concepts, Mechanisms, and Challenges, Advanced Materials. 31 (2019). https://doi.org/10.1002/adma.201901997.

[13] M. Bellardita, R. Fiorenza, L. D'urso, L. Spitaleri, A. Gulino, G. Compagnini, S. Scirè, L. Palmisano, Exploring the photothermo-catalytic performance of brookite tio2-ceo2 composites, Catalysts. 10 (2020). https://doi.org/10.3390/catal10070765.

[14] X. Lang, W. Ma, C. Chen, H. Ji, J. Zhao, Selective aerobic oxidation mediated by TiO2 photocatalysis, Acc Chem Res. 47 (2014) 355–363. https://doi.org/10.1021/ar4001108.

[15] X. Li, J.L. Shi, H. Hao, X. Lang, Visible light-induced selective oxidation of alcohols with air by dye-sensitized TiO2 photocatalysis, Appl Catal B. 232 (2018) 260–267. https://doi.org/10.1016/j.apcatb.2018.03.043.

[16] R. Bagtache, K. Boudjedien, A.M. Djaballah, M. Trari, Phototoelectrochemical characterization of Ag/ CuCo2O4 prepared at low temperature: application to solar light oxidation of methyl orange, International Journal of Environmental Science and Technology. 19 (2022) 9957–9966. https://doi.org/10.1007/s13762-021-03832-y.

[17] M.A. Marwat, H. Ullah, M. Usman, M.A. Ehsan, H. Zhang, M.F. Khan, S. Ali, M. Yousaf, Significantly improved photocatalytic activity of the SnO2/BiFeO3 heterojunction for pollutant degradation and mechanism, Ceram Int. 48 (2022) 14789–14798. https://doi.org/10.1016/j.ceramint.2022.02.016.

[18] M. Sabri, A. Habibi-Yangjeh, S. Ghosh, Novel ZnO/CuBi2O4 heterostructures for persulfate-assisted photocatalytic degradation of dye contaminants under visible light, J Photochem Photobiol A Chem. 391 (2020). https://doi.org/10.1016/j.jphotochem.2020.112397.

[19] S. Pulipaka, N. Boni, G. Ummethala, P. Meduri, CuO/CuBi2O4 heterojunction photocathode: High stability and current densities for solar water splitting, J Catal. 387 (2020) 17–27. https://doi.org/10.1016/j.jcat.2020.04.001.

[20] O. Mertah, A. Gómez-Avilés, A. Kherbeche, C. Belver, J. Bedia, Peroxymonosulfate enhanced photodegradation of sulfamethoxazole with TiO2@CuCo2O4catalysts under simulated solar light, J Environ Chem Eng. 10 (2022). https://doi.org/10.1016/j.jece.2022.108438.

[21] J. Zhang, Y. Jiang, W. Gao, H. Hao, Synthesis and visible photocatalytic activity of new photocatalyst MBi2O4(M = Cu, Zn), Journal of Materials Science: Materials in Electronics. 26 (2015) 1866–1873. https://doi.org/10.1007/s10854-014-2622-7.

[22] R. Li, T. Li, Q. Zhou, Impact of titanium dioxide (TiO2) modification on its application to pollution treatment—a review, Catalysts. 10 (2020). https://doi.org/10.3390/catal10070804.

[23] R. Fiorenza, M. Bellardita, T. Barakat, S. Scirè, L. Palmisano, Visible light photocatalytic activity of macro-mesoporous TiO2-CeO2 inverse opals, J Photochem Photobiol A Chem. 352 (2018) 25–34. https://doi.org/10.1016/j.jphotochem.2017.10.052.

[24] Q. Shi, G. Ping, X. Wang, H. Xu, J. Li, J. Cui, H. Abroshan, H. Ding, G. Li, CuO/TiO 2 heterojunction composites: An efficient photocatalyst for selective oxidation of methanol to methyl formate, J Mater Chem A Mater. 7 (2019) 2253–2260. https://doi.org/10.1039/c8ta09439j.

[25] Y. Wang, H. Wang, T. He, Study on nanoporous CuBi2O4 photocathode coated with TiO2 overlayer for photoelectrochemical CO2 reduction, Chemosphere. 264 (2021). https://doi.org/10.1016/j.chemosphere.2020.128508.

[26] C. van Tran, D.D. La, P.N. Thi Hoai, H.D. Ninh, P.N. Thi Hong, T.H.T. Vu, A.K. Nadda, X.C. Nguyen, D.D. Nguyen, H.H. Ngo, New TiO2-doped Cu–Mg spinel-ferrite-based photocatalyst for degrading highly toxic rhodamine B dye in wastewater, J Hazard Mater. 420 (2021). https://doi.org/10.1016/j.jhazmat.2021.126636.

[27] R. Brahimi, Y. Bessekhouad, A. Bouguelia, M. Trari, CuAlO2/TiO2 heterojunction applied to visible light H2 production, J Photochem Photobiol A Chem. 186 (2007) 242–247. https://doi.org/10.1016/j.jphotochem.2006.08.013.

[28] A.F. Shojaei, A.R. Tabari, M.H. Loghmani, Normal spinel CoCr2O4 and CoCr2O 4/TiO2 nanocomposite as novel photocatalysts, for degradation of dyes, Micro Nano Lett. 8 (2013) 426–431. https://doi.org/10.1049/mnl.2013.0114.

[29] H. Lahmar, M. Benamira, F.Z. Akika, M. Trari, Reduction of chromium (VI) on the hetero-system CuBi2O4/TiO2 under solar light, Journal of Physics and Chemistry of Solids. 110 (2017) 254–259. https://doi.org/10.1016/j.jpcs.2017.06.021.

[30] N.T.M. Tho, B.T. Huy, D.N.N. Khanh, H.N.N. Ha, V.Q. Huy, N.T.T. Vy, D.M. Huy, D.P. Dat, N.T.K. Phuong, Facile synthesis of ZnBi2O4-graphite composites as highly active visible-light photocatalyst for the mineralization of rhodamine B, Korean Journal of Chemical Engineering. 35 (2018) 2442–2451. https://doi.org/10.1007/s11814-018-0156-z.

[31] C.M. Pecoraro, M. Bellardita, V. Loddo, F. di Franco, L. Palmisano, M. Santamaria, A facile way to synthesize noble metal free TiO2 based catalysts for glycerol photoreforming, Journal of Industrial and Engineering Chemistry. (2022). https://doi.org/10.1016/j.jiec.2022.11.010.

[32] R. Fiorenza, M. Bellardita, S. Scirè, L. Palmisano, Photocatalytic H2 production over inverse opal TiO2 catalysts, Catal Today. (2019) 113–119. https://doi.org/10.1016/j.cattod.2017.12.011.

[33] M.M. Ba-Abbad, A.H. Amir Kadhum, A. Bakar Mohamad, M.S. Takriff, K. Sopian, D. Ehsan, Synthesis and Catalytic Activity of TiO 2 Nanoparticles for Photochemical Oxidation of Concentrated Chlorophenols under Direct Solar Radiation, 2012. www.electrochemsci.org.

[34] R. López, R. Gómez, Band-gap energy estimation from diffuse reflectance measurements on sol-gel and commercial TiO 2: A comparative study, J Solgel Sci Technol. 61 (2012) 1–7. https://doi.org/10.1007/s10971-011-2582-9.

[35] N. Serpone, Is the band gap of pristine TiO2 narrowed by anion- and cation-doping of titanium dioxide in second-generation photocatalysts?, Journal of Physical Chemistry B. 110 (2006) 24287–24293. https://doi.org/10.1021/jp065659r.

[36] Y.C. Nah, I. Paramasivam, P. Schmuki, Doped TiO2 and TiO2 nanotubes: Synthesis and applications, ChemPhysChem. 11 (2010) 2698–2713. https://doi.org/10.1002/cphc.201000276.

[37] N.R. Khalid, E. Ahmed, N.A. Niaz, G. Nabi, M. Ahmad, M.B. Tahir, M. Rafique, M. Rizwan, Y. Khan, Highly visible light responsive metal loaded N/TiO2 nanoparticles for photocatalytic conversion of CO2 into methane, Ceram Int. 43 (2017) 6771–6777. https://doi.org/10.1016/j.ceramint.2017.02.093.

[38] D. Fang, F. He, J. Xie, L. Xue, Calibration of Binding Energy Positions with C1s for XPS Results, Journal Wuhan University of Technology, Materials Science Edition. 35 (2020) 711–718. https://doi.org/10.1007/s11595-020-2312-7.

[39] P. Krishnan, M. Liu, P.A. Itty, Z. Liu, V. Rheinheimer, M.H. Zhang, P.J.M. Monteiro, L.E. Yu, Characterization of photocatalytic TiO2 powder under varied environments using near ambient pressure X-ray photoelectron spectroscopy, Sci Rep. 7 (2017). https://doi.org/10.1038/srep43298.

[40] B. Bharti, S. Kumar, H.N. Lee, R. Kumar, Formation of oxygen vacancies and Ti3+ state in TiO2 thin film and enhanced optical properties by air plasma treatment, Sci Rep. 6 (2016). https://doi.org/10.1038/srep32355.

[41] J.K. Cooper, Z. Zhang, S. Roychoudhury, C.M. Jiang, S. Gul, Y.S. Liu, R. Dhall, A. Ceballos, J. Yano, D. Prendergast, S.E. Reyes-Lillo, CuBi2O4: Electronic Structure, Optical Properties, and Photoelectrochemical Performance Limitations of the Photocathode, Chemistry of Materials. 33 (2021) 934–945. https://doi.org/10.1021/acs.chemmater.0c03930.

[42] G. Avgouropoulos, T. Ioannides, Selective CO oxidation over CuO-CeO 2 catalysts prepared via the urea-nitrate combustion method, 2002.

[43] N. Ohtsu, N. Masahashi, Y. Mizukoshi, K. Wagatsuma, Hydrocarbon decomposition on a hydrophilic TiO2 surface by UV irradiation: Spectral and quantitative analysis using in-situ XPS technique, Langmuir. 25 (2009) 11586–11591. https://doi.org/10.1021/la901505m.

[44] A. Zaffora, F. di Franco, F. di Quarto, M. Santamaria, Optimization of anodizing process of tantalum for Ta2O5-based capacitors, Journal of Solid State Electrochemistry. 24 (2020) 2953–2962. https://doi.org/10.1007/s10008-020-04704-0.

[45] A. di Paola, M. Bellardita, B. Megna, F. Parrino, L. Palmisano, Photocatalytic oxidation of trans-ferulic acid to vanillin on TiO2 and WO3-loaded TiO2 catalysts, Catal Today. 252 (2015) 195–200. https://doi.org/10.1016/j.cattod.2014.09.012.

[46] F. Parrino, S.F. Corsino, M. Bellardita, V. Loddo, L. Palmisano, M. Torregrossa, G. Viviani, Sequential biological and photocatalysis based treatments for shipboard slop purification: A pilot plant investigation, Process Safety and Environmental Protection. 125 (2019) 288–296. https://doi.org/10.1016/j.psep.2019.03.025.

[47] M. Bellardita, C. Garlisi, L.Y. Ozer, A.M. Venezia, J. Sá, F. Mamedov, L. Palmisano, G. Palmisano, Highly stable defective TiO2-x with tuned exposed facets induced by fluorine: Impact of surface and bulk properties on selective UV/visible alcohol photo-oxidation, Appl Surf Sci. 510 (2020). https://doi.org/10.1016/j.apsusc.2020.145419.

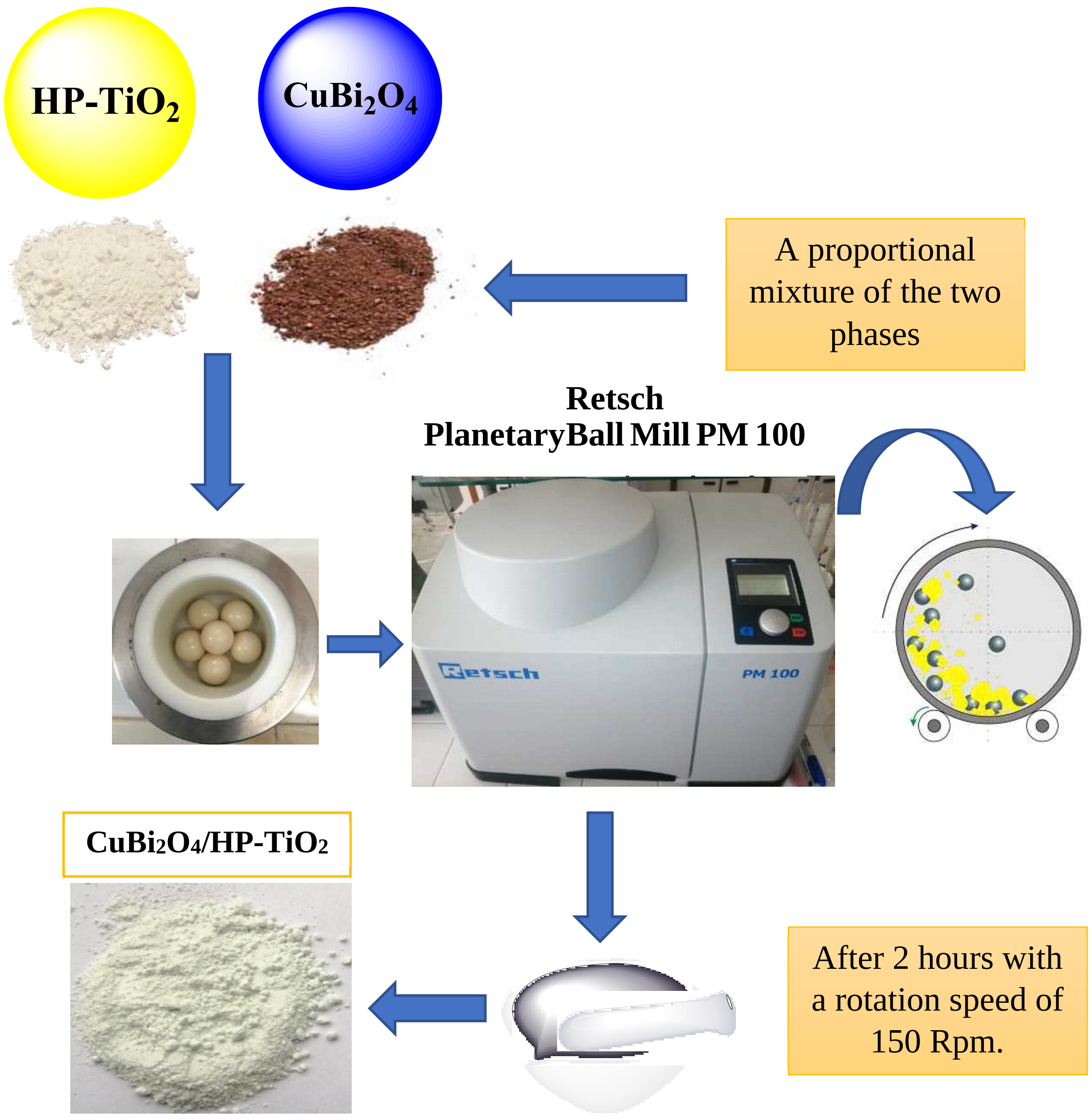


**Fig 1.** Preparation of $CuBi_2O_4$/HP-$TiO_2$ by ball milling.

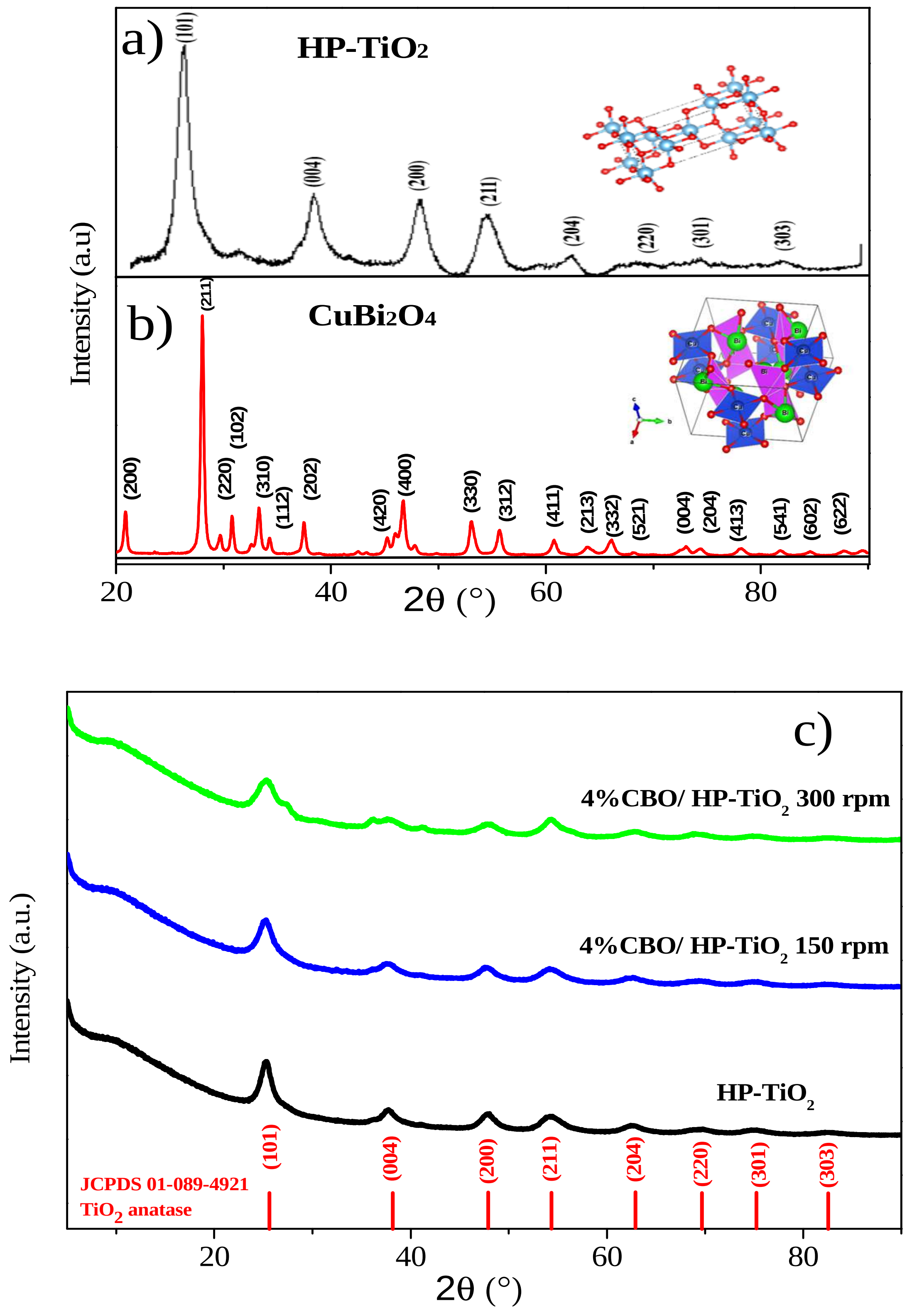


**Fig. 2.** a) XRD patterns of (a) $CuBi_2O_4$, (b) HP-$TiO_2$, (c) 4% CBO/ HP-$TiO_2$ hetero-systems prepared at 150 rpm and 300 rpm, and bare HP-$TiO_2$.

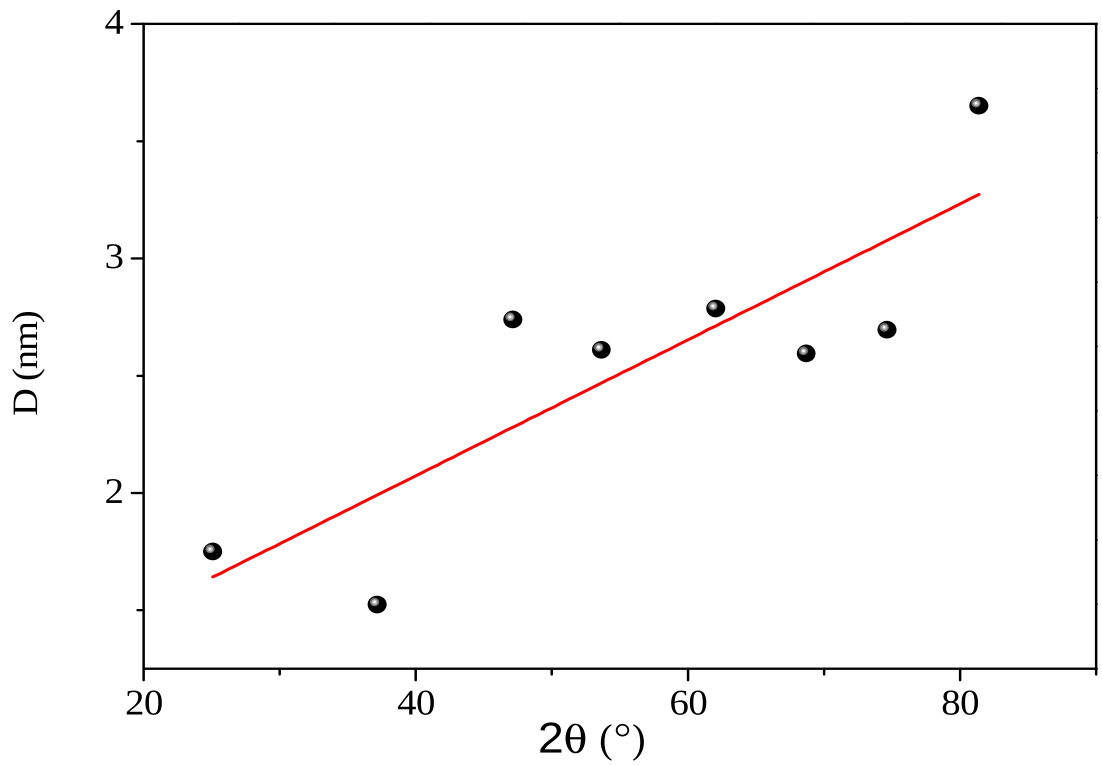


**Fig 3**. The crystallite size of 4% $CuBi_2O_4$/ HP-$TiO_2$ determined from the Williamson–Hall plot.

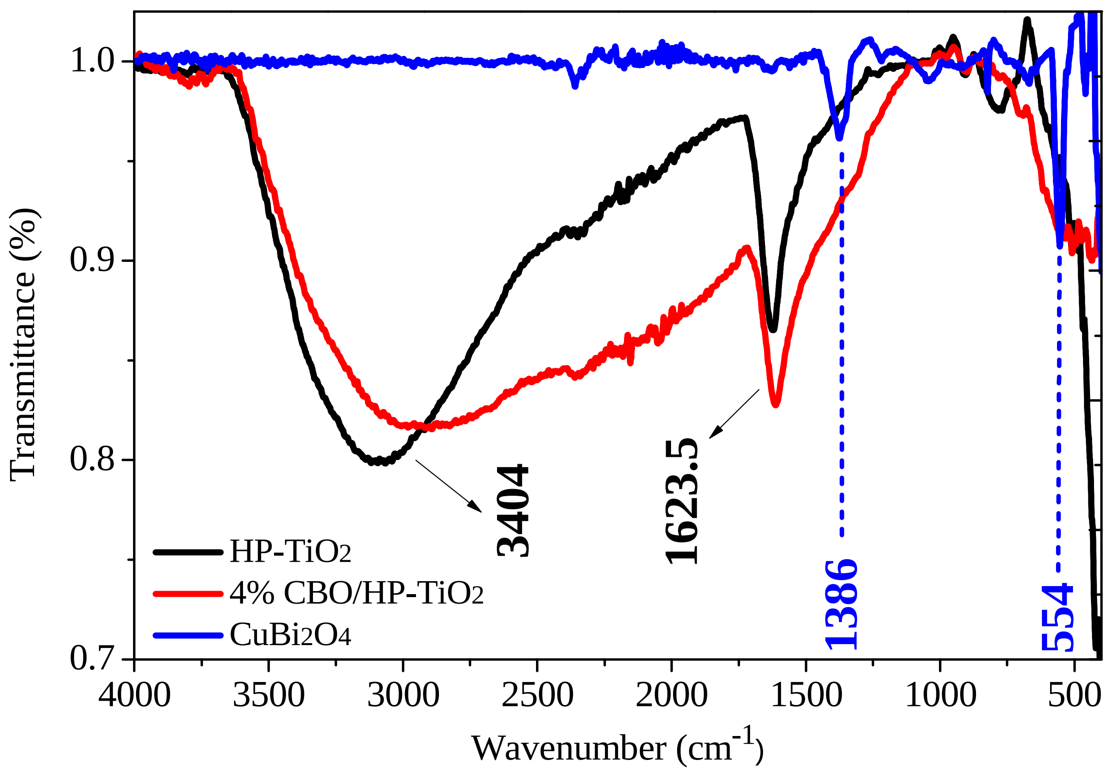


**Fig 4.** The FTIR spectrum of $CuBi_2O_4$, HP-$TiO_2$ and 4% $CuBi_2O_4$/HP-$TiO_2$.

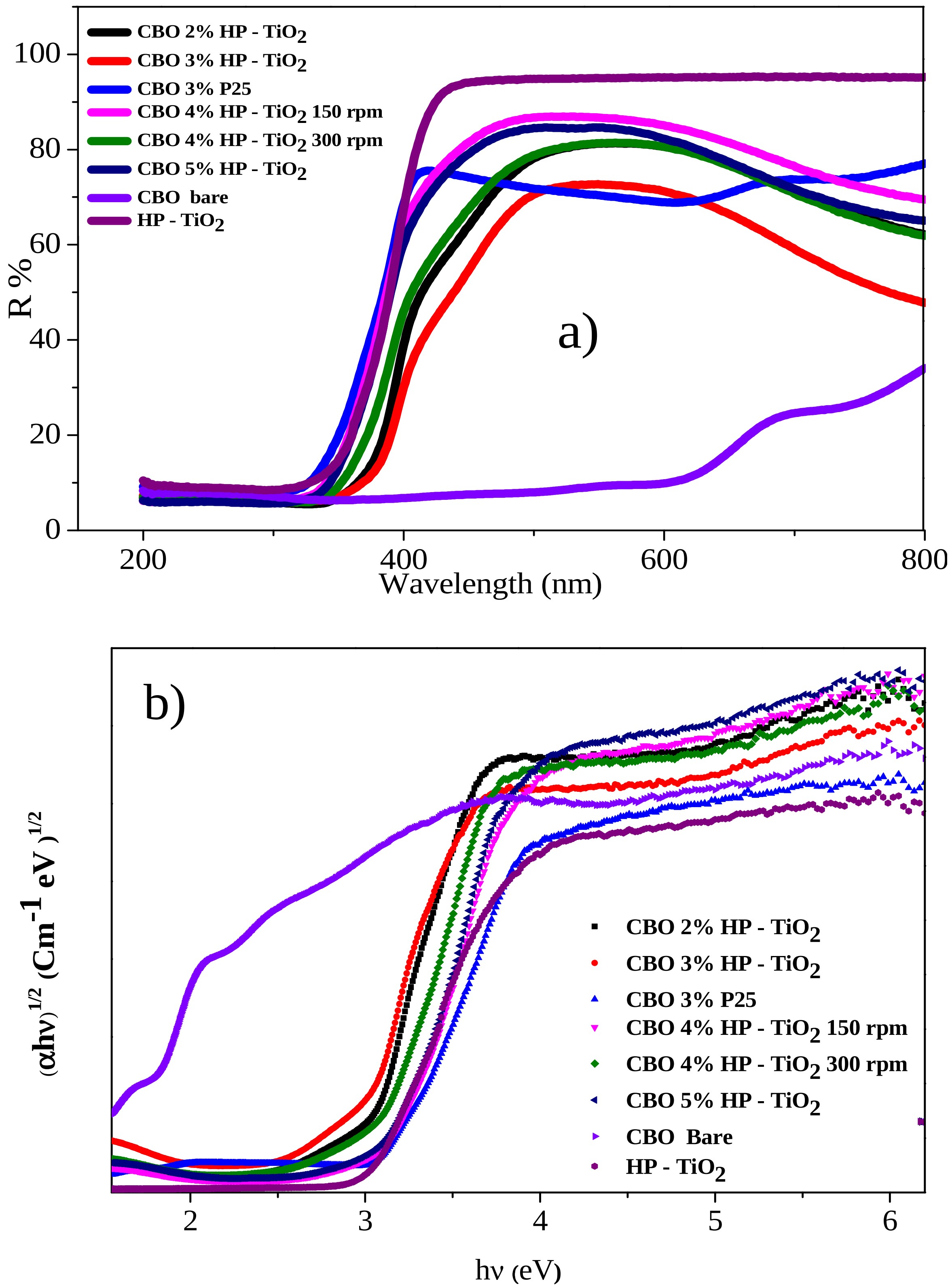


**Fig. 5**. (a) The UV–Vis diffuse reflectance spectra; (b) Tauc plot of all the used samples.

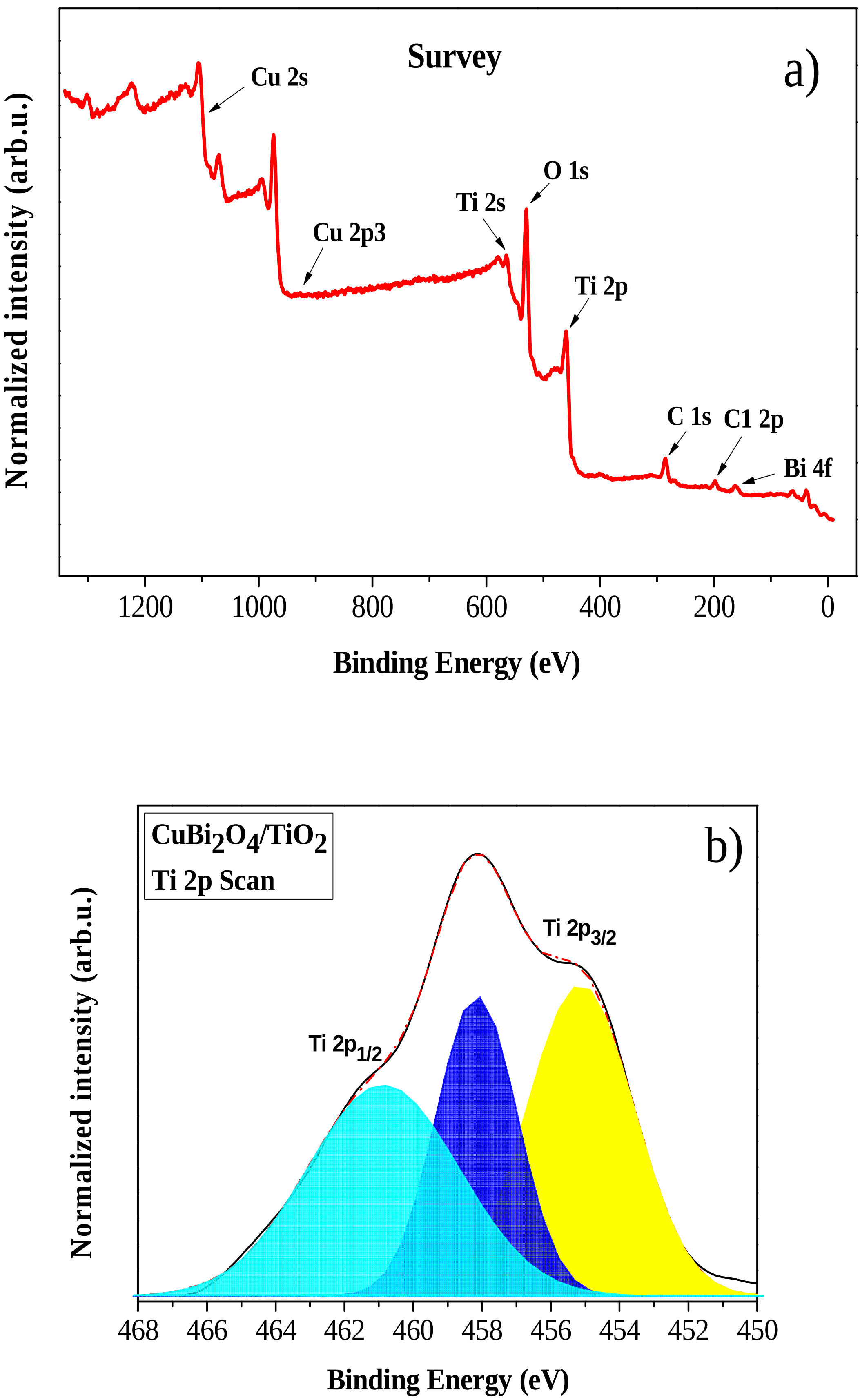

Survey
a)
Cu 2s
Cu 2p3
Ti 2s
O 1s
Ti 2p
C 1s
C1 2p
Bi 4f
Normalized intensity (arb.u.)
1200
1000
800
600
400
200
0
Binding Energy (eV)
b)
$CuBi_2O_4/TiO_2$
Ti 2p Scan
Ti $2p_{3/2}$
Ti $2p_{1/2}$
Normalized intensity (arb.u.)
468
466
464
462
460
458
456
454
452
450
Binding Energy (eV)

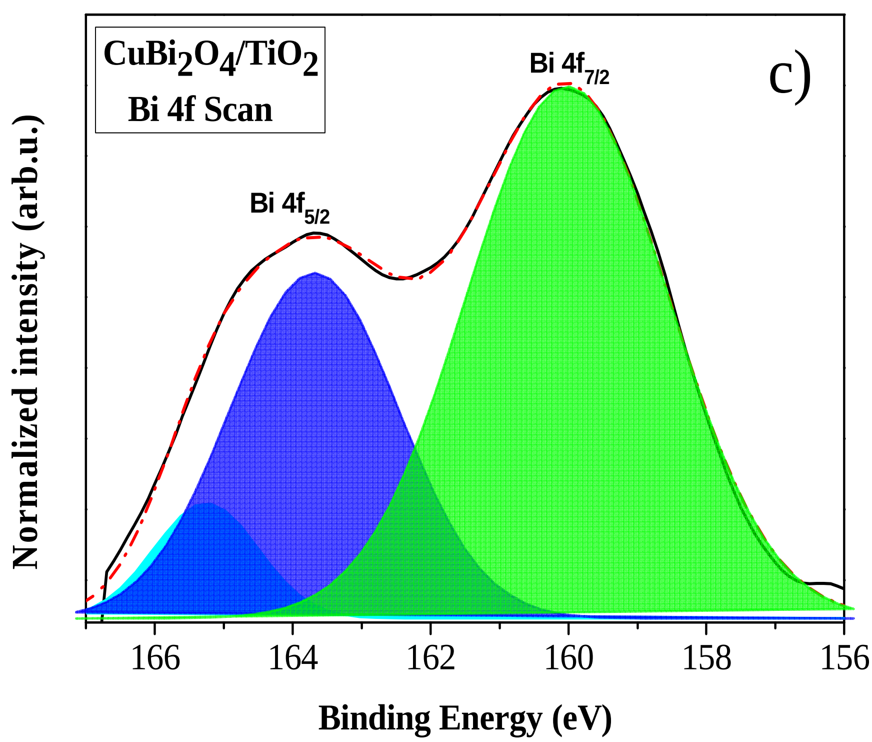
CuBi2O4/TiO2
Bi 4f Scan
c)
Bi 4f7/2
Bi 4f5/2
Normalized intensity (arb.u.)
166
164
162
160
158
156
Binding Energy (eV)

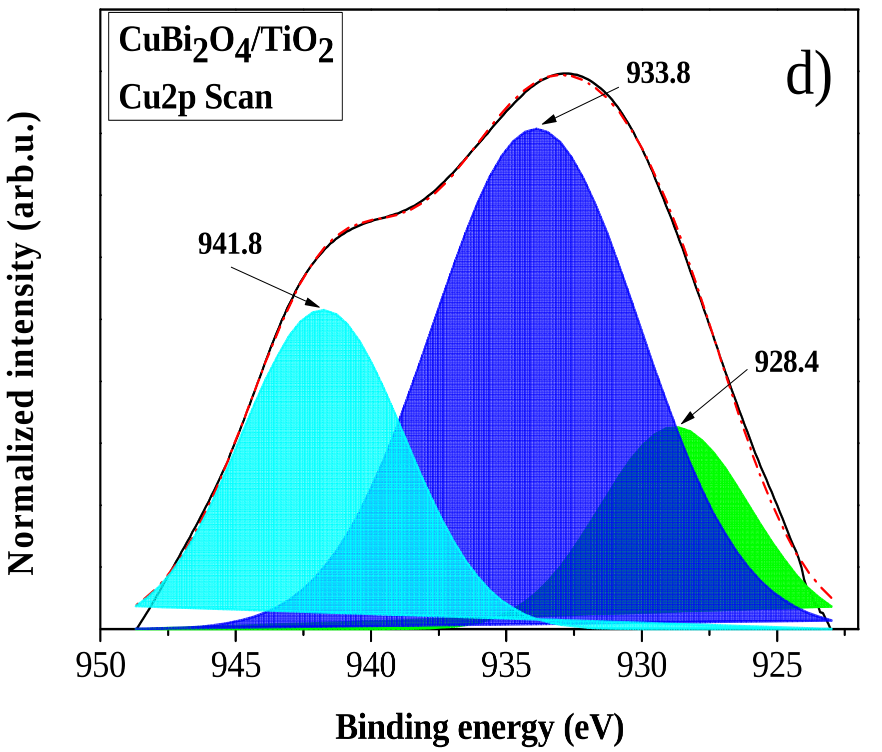
CuBi2O4/TiO2
Cu2p Scan
d)
933.8
941.8
928.4
Normalized intensity (arb.u.)
950
945
940
935
930
925
Binding energy (eV)

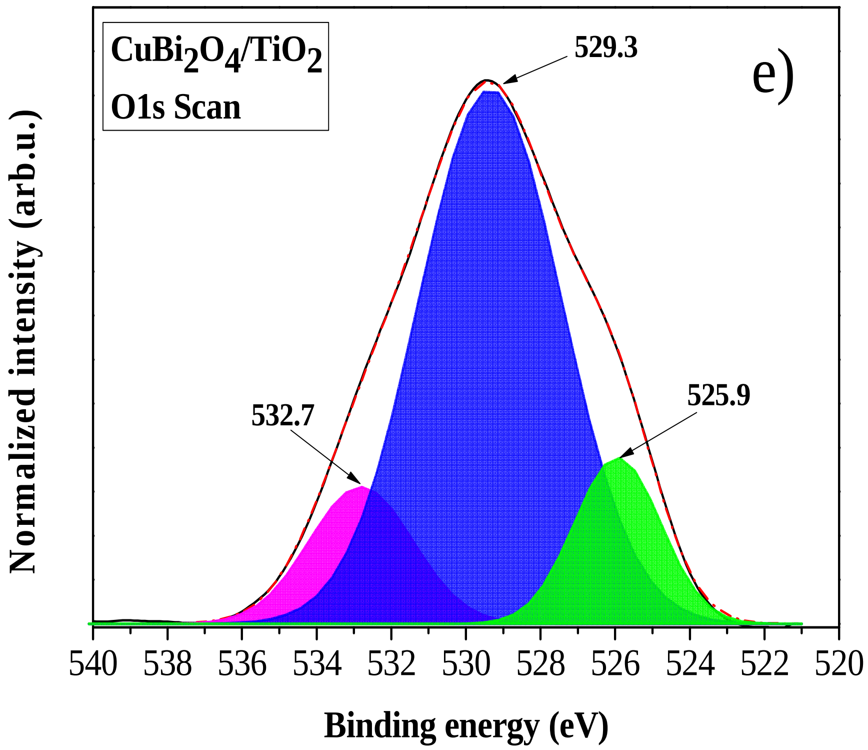


**Fig. 6**. XPS spectra survey of 4% $CuBi_2O_4$/HP-$TiO_2$. (a) XPS survey spectra, (b) Ti 2p, (c) Bi 4f, (d) Cu 2p, (e) O 1s XPS spectra.

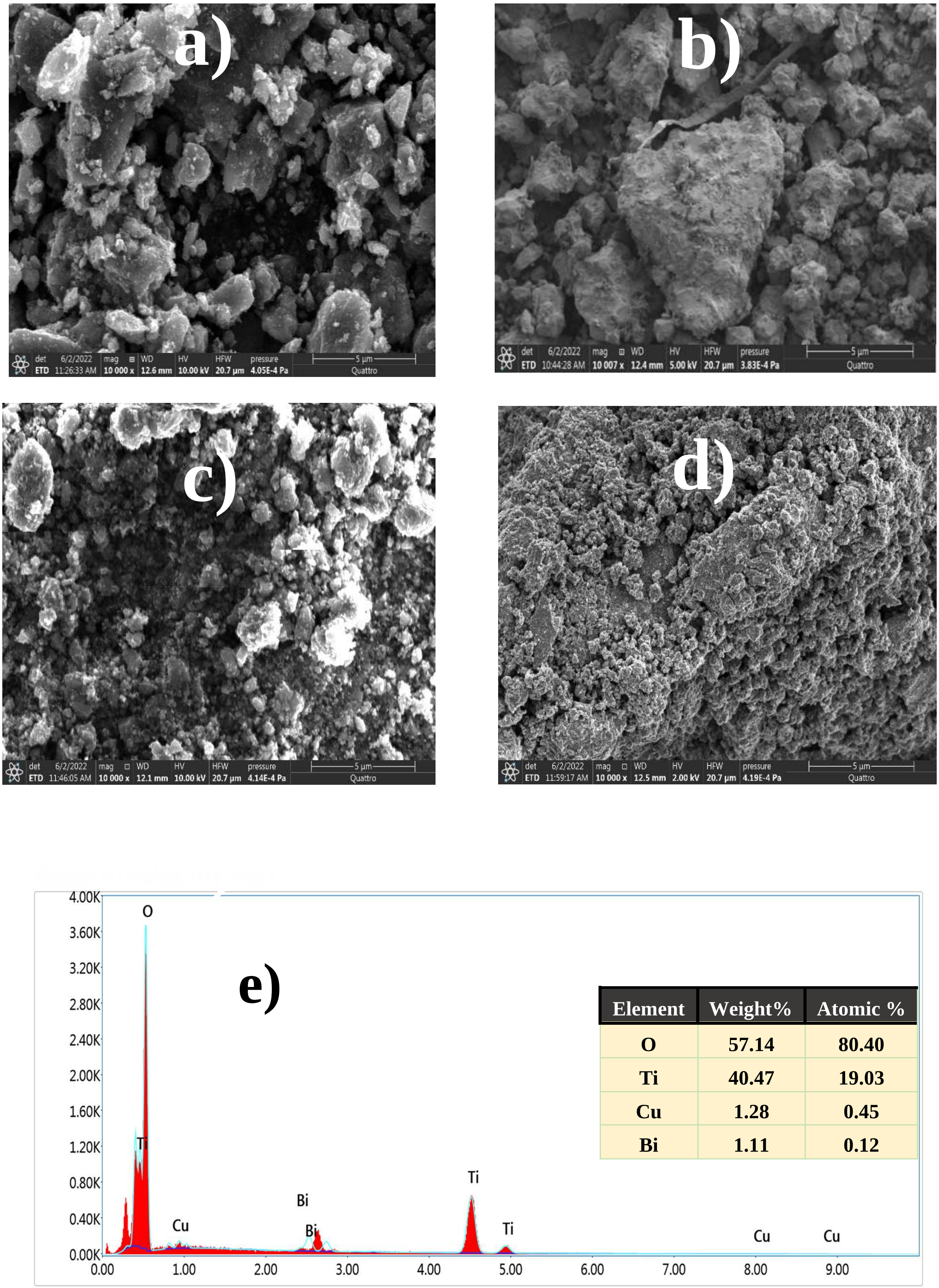


| Element | Weight% | Atomic % |
|---|---|---|
| O | 57.14 | 80.40 |
| Ti | 40.47 | 19.03 |
| Cu | 1.28 | 0.45 |
| Bi | 1.11 | 0.12 |

**f)**

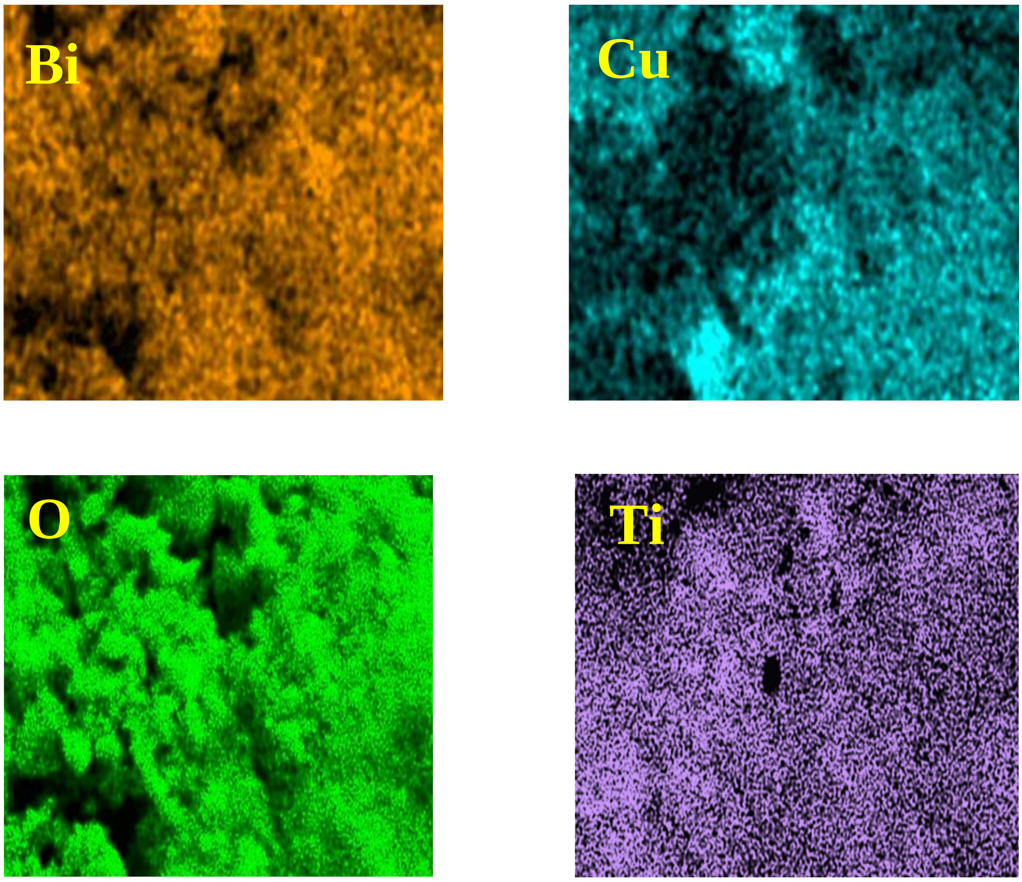


**Fig. 7.** SEM images of the samples: (a) bare HP-$TiO_2$, (b) bare CBO (c) 4% CBO/HP-$TiO_2$ 150 rpm and (d) 4% CBO/HP-$TiO_2$ 300 rpm, (e) EDS spectra of 4% CBO/HP-$TiO_2$ 150 rpm, (f) the EDS elemental mapping images of 4% CBO/HP-$TiO_2$ 150 rpm.

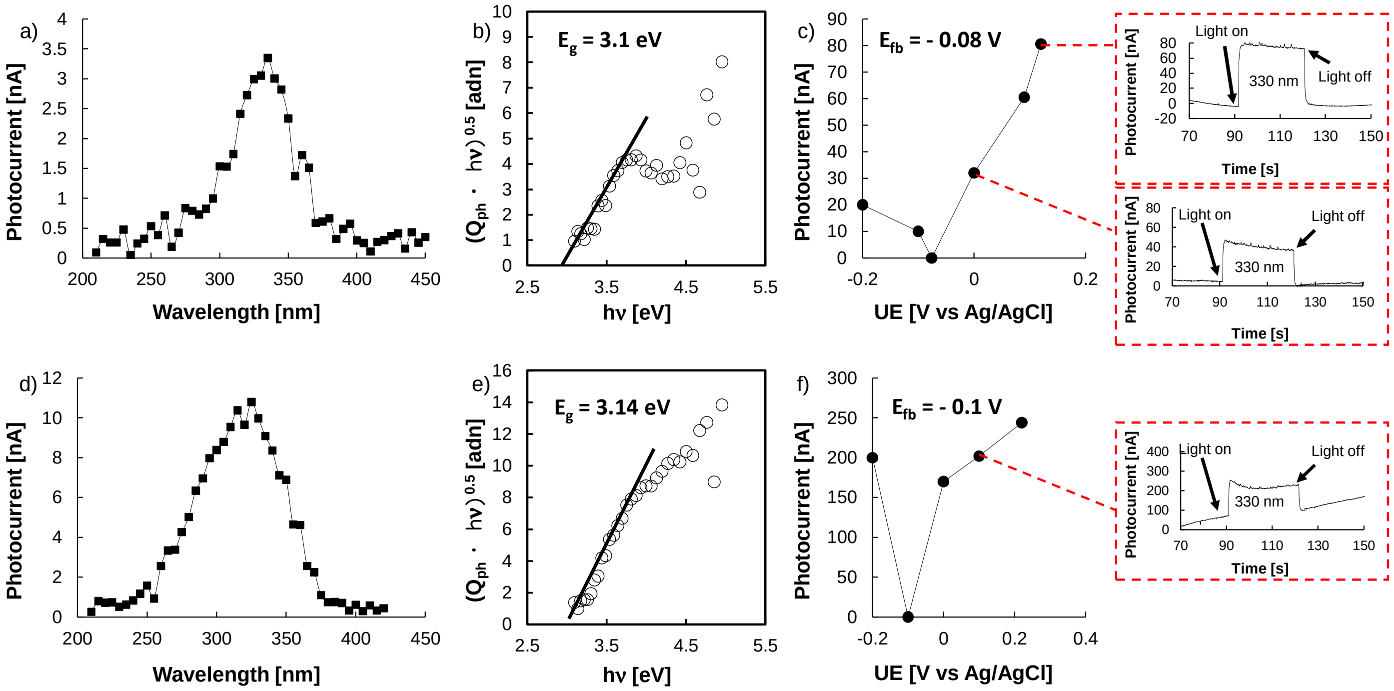


**Fig. 8.** Photocurrent spectra of HP-$TiO_2$ and 4% CBO/ HP-$TiO_2$ recorded in 0.1 M ABE and UE of 0.12 V and 0.22 V vs/Ag/AgCl respectively are reported in a) and d). The respective $(Q_{ph} \cdot h\nu)^{0.5}$ vs hν plots are shown in b) and e). Current transient under monochromatic light recorded at 330 nm are reported in c) and f), respective photocurrent vs time plot are reported in the inset.

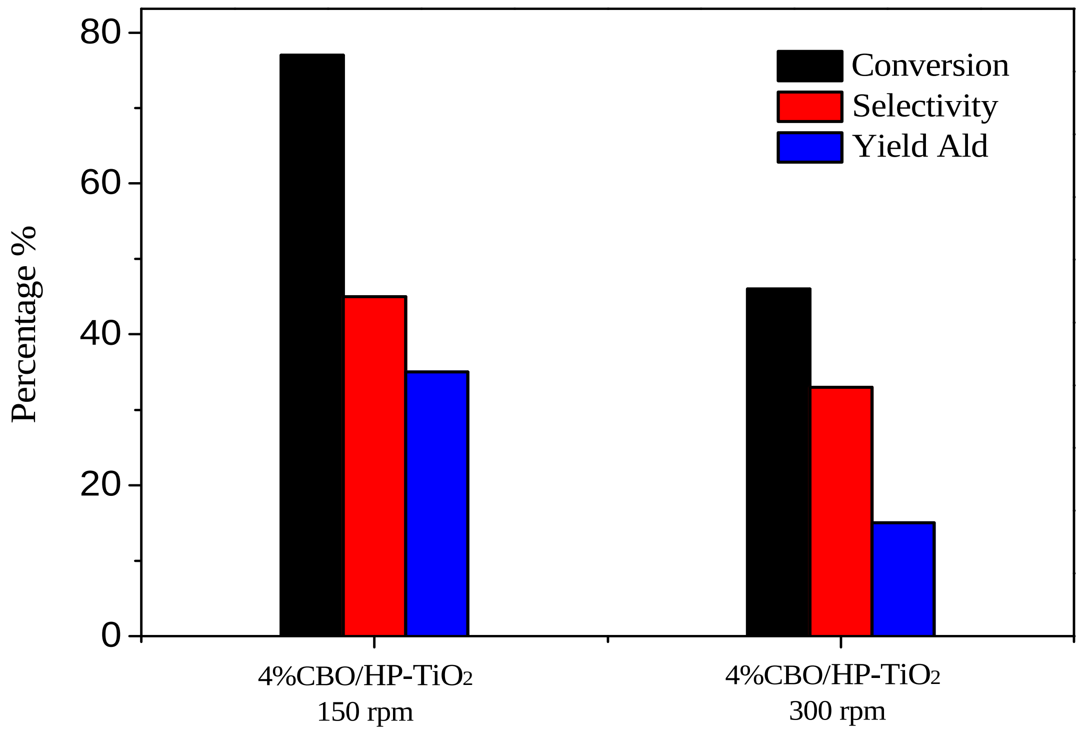


**Fig. 9.** Comparison of photocatalytic performance towards the selective oxidation of 4-methoxybenzyl alcohol by using the 4% CBO/HP-$TiO_2$ junction prepared at 150 and 300 rpm.

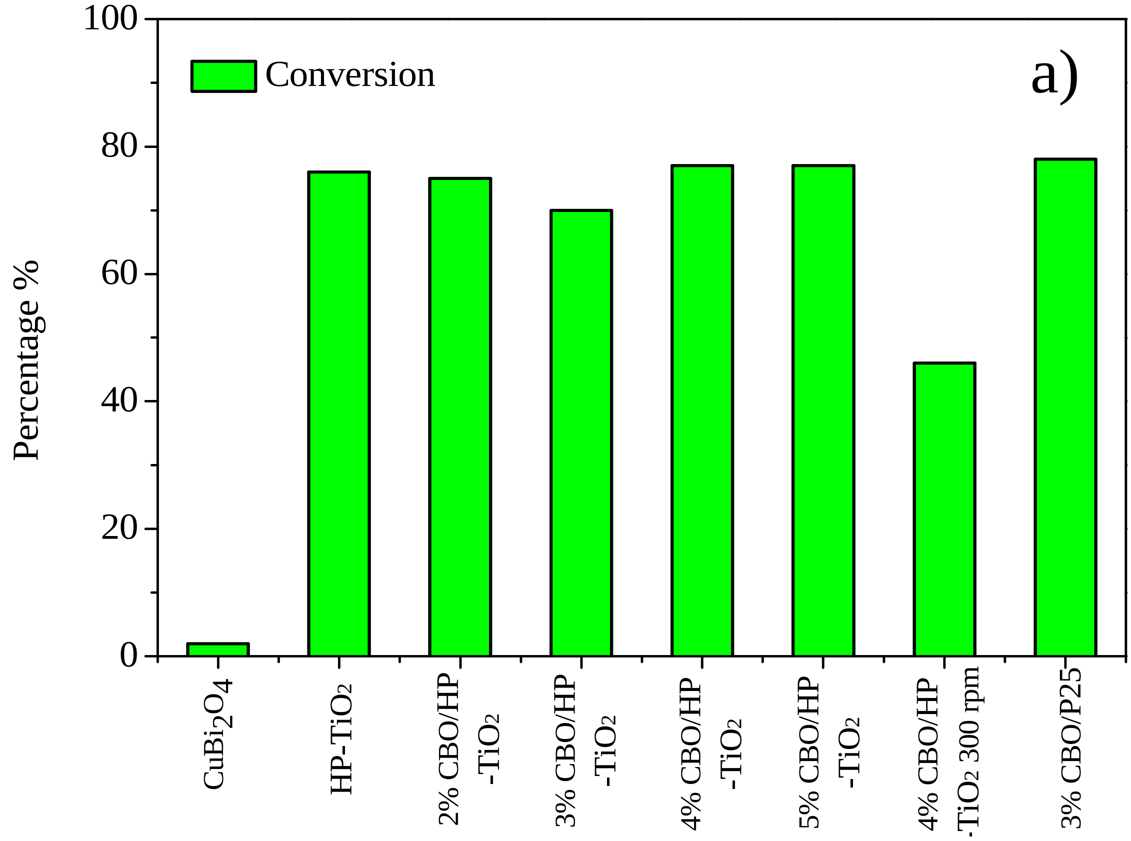

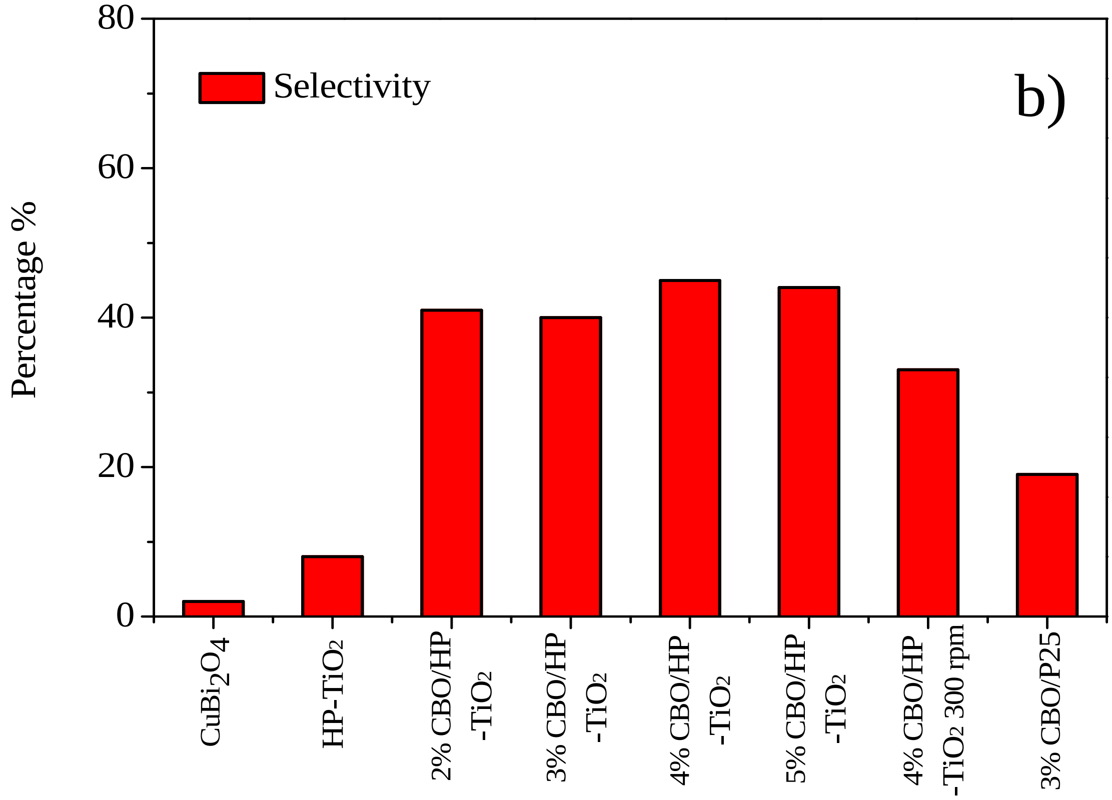


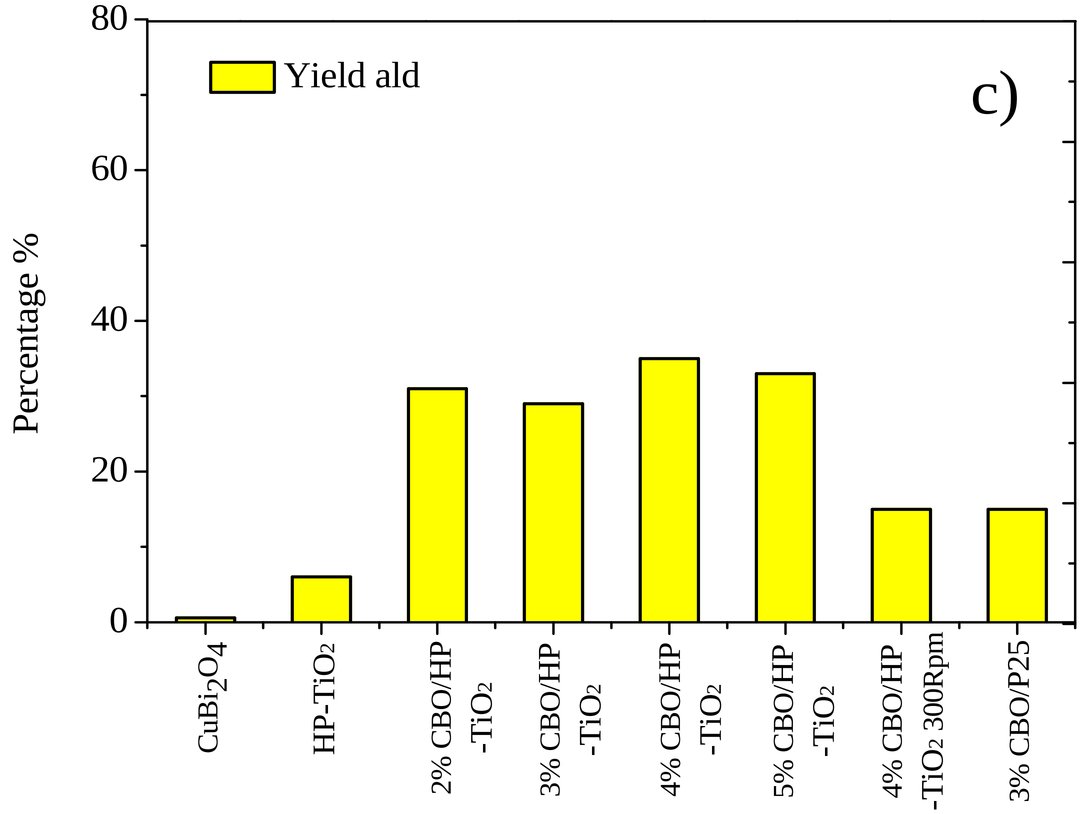


**Fig. 10.** Photocatalytic performance of the different CBO/HP-$TiO_2$ coupled samples and bare CBO and HP-$TiO_2$ under irradiation for 4 h towards 4-MBA oxidation in term of Conversion (a), Selectivity (b) and Yield (c).

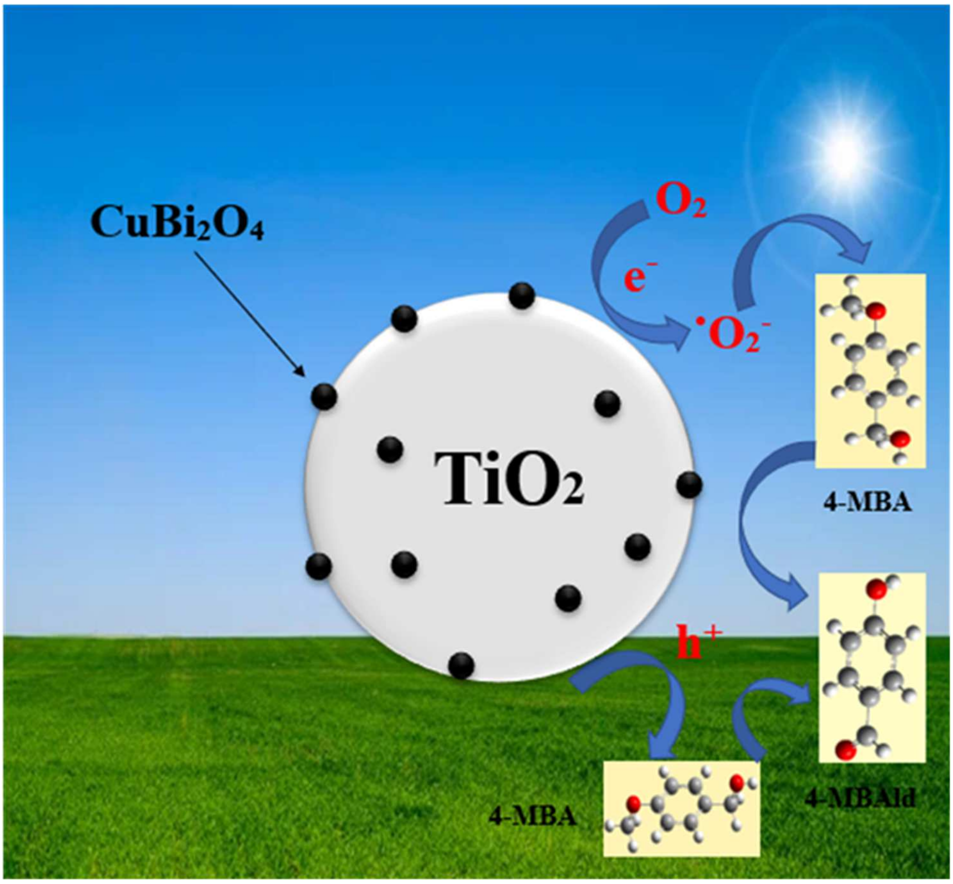


**Fig. 11**. Proposed mechanism for selective oxidation of 4-MBA to 4-MBald using $CuBi_2O_4$/HP-$TiO_2$ photocatalysts under simulated solar light irradiation.